GEOPHYSICS, VOL. 82, NO. 6 (NOVEMBER-DECEMBER 2017); P. ID35–ID44, 12 FIGS.
10.1190/GEO2017-0044.1

Check for updates

Downloaded 03/25/20 to 73.151.200.131. Redistribution subject to SEG license or copyright; see Terms of Use at http://library.seg.org/

Lithology-controlled stress variations and pad-scale faults: A case study of hydraulic fracturing in the Woodford Shale, Oklahoma

Xiaodong Ma[1] and Mark D. Zoback[1]

ABSTRACT

We have conducted an integrated study to investigate the petrophysical and geomechanical factors controlling the effectiveness of hydraulic fracturing (HF) in four subparallel horizontal wells in the Mississippi Limestone-Woodford Shale (MSSP-WDFD) play in Oklahoma. In two MSSP wells, the minimum horizontal stress $S_{h\ min}$ indicated by the instantaneous shut-in pressures of the HF stages are significantly less than the vertical stress S_v. This, combined with observations of drilling-induced tensile fractures in the MSSP in a vertical well at the site, indicates that this formation is in a normal/strike-slip faulting stress regime, consistent with earthquake focal mechanisms and other stress indicators in the area. However, the $S_{h\ min}$ values are systematically higher and vary significantly from stage to stage in two WDFD wells. The stages associated with the abnormally high $S_{h\ min}$ values (close to S_v) were associated with little to no proppant placement and a limited number of microseismic events. We used compositional logs to determine the content of compliant components (clay and kerogen). Due to small variations in the trajectories of the horizontal wells, they penetrated three thin, but compositionally distinct WDFD lithofacies. We found that $S_{h\ min}$ along the WDFD horizontals increases when the stage occurred in a zone with high clay and kerogen content. These variations of $S_{h\ min}$ can be explained by various degrees of viscous stress relaxation, which results in the increase in $S_{h\ min}$ (less stress anisotropy), as the compliant component content increases. The distribution of microseismic events was also affected by normal and strike-slip faults cutting across the wells. The locations of these faults were consistent with unusual lineations of microseismic events and were confirmed by 3D seismic data. Thus, the overall effectiveness of HF stimulation in the WDFD wells at this site was strongly affected the abnormally high HF gradients in clay-rich lithofacies and the presence of preexisting, pad-scale faults.

INTRODUCTION

The Mississippi Limestone (MSSP) is a relatively shallow (4000–7000 ft depth) carbonate formation that spans much of northern Oklahoma and southern Kansas. The organic-rich Woodford Shale (WDFD) immediately underlies the MSSP, and it is considered to be the MSSP source rock. It is now common to drill subparallel horizontal wells in the MSSP and WDFD at a given location to exploit the stacked pay. Highly variable performance of wells in the WDFD formation is an ongoing challenge. To address this, we conducted an integrated study of a pair of stacked horizontal wells to investigate the effectiveness of multistage hydraulic fracturing (HF) from a multidisciplinary perspective (Ma and Zoback, 2017). The study area consists of four subparallel horizontal wells (A, B, C, and D) covering approximately 1 mi^2 (Figure 1). Two wells were drilled in the MSSP (wells A and C) and two close to the top of the WDFD formation (wells B and D). Three vertical observation wells (I, II, and III) were drilled for microseismic monitoring. A comprehensive set of geophysical logs was obtained in well II.

The focus of our analysis is to better understand the variable effectiveness of stimulation in the two WDFD horizontal wells. The horizontal section of each well was approximately 5000 ft long and stimulated with up to 15 HF stages. In this paper, we first present the development of a geomechanical model of the study area. We then examine the relationships between in situ stress conditions along the laterals, and their relation to lithology variations within the WDFD. Finally, we address the role of preexisting, cross-cutting faults on the effectiveness of HF stimulation.

Manuscript received by the Editor 20 January 2017; revised manuscript received 8 June 2017; published ahead of production 28 August 2017; published online 23 October 2017.
[1]Stanford University, Department of Geophysics, Stanford, California, USA. E-mail: xiaodongma.rocks@gmail.com; zoback@stanford.edu.
© 2017 Society of Exploration Geophysicists. All rights reserved.

Downloaded 03/25/20 to 73.151.200.131. Redistribution subject to SEG license or copyright; see Terms of Use at http://library.seg.org/

GEOMECHANICAL MODEL OF THE STUDY AREA

To develop a geomechanical model, we constrained the in situ state of stress in the study area following methods described by Zoback (2007). The overburden stress S_V was determined by integrating the density log obtained in well II. As confirmed by the orientations of drilling-induced tensile fractures (DITFs) in the well (described below), the overburden stress appears to be perpendicular to the earth's surface. The S_V profile with depth is shown by the black line in Figure 2. Based on the measurements taken in well II, pore pressure P_p is slightly less than hydrostatic below the WDFD formation, which is consistent with the regional data (Nelson and Gianoutsos, 2014). The direction of the maximum horizontal stress $S_{H\ max}$ is approximately east–west, which is inferred from the fast-shear velocity azimuth obtained from dipole sonic logs from vertical wells near the study area. As shown in Figure 3, the $S_{H\ max}$ direction is reasonably consistent among all the wells. The stress orientations shown in Figure 3 agree with the regional $S_{H\ max}$ direction as shown by Alt and Zoback (2017) principally using the orientations of DITFs in vertical wells in the region and confirmed by earthquake focal mechanisms. As shown in Figure 4 from a nearby vertical well in this area, the DITFs strike east–west within the MSSP, consistent with the fast-shear velocity direction.

Information on the magnitude of $S_{h\ min}$ is available from several sources. The function $S_{h\ min}$ (which is the least principal stress S_3 in

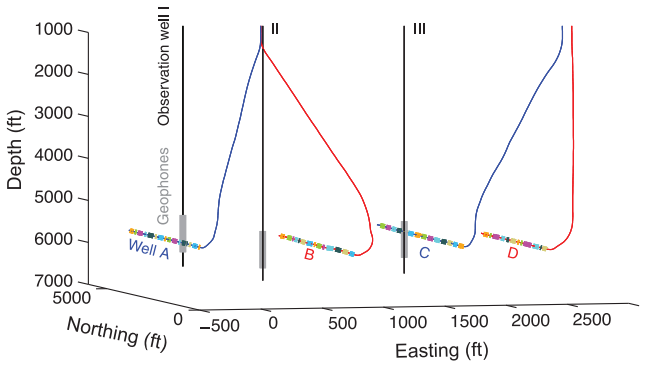

Figure 1. The configuration of four horizontal wells (A, B, C, and D) and three vertical observation wells (I, II, and III) in the study area. The positions of the HF stages in wells A, B, C, D and geophone arrays in vertical wells I, II, and III. All three arrays recorded each of the 12–15 HF stages in the four horizontal wells.

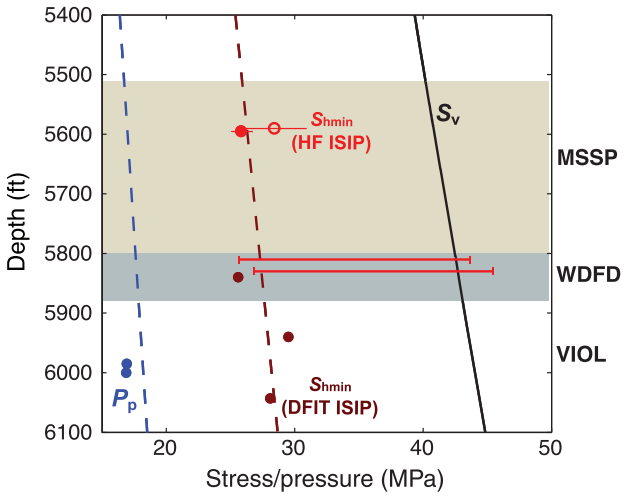

Figure 2. Stress and pore pressure in the study area. The hydrostatic pore pressure gradient (blue dashed line) and $S_{h\ min}$ gradient (dashed brown line) based on DFITs in the Viola Formation is shown by brown dots, and hydraulic fractures in the MSSP are shown by red dots (solid: well C; open: well A). The solid red bars in the WDFD represent the range of ISIPs of the individual HF stages in wells B (upper) and D (lower).

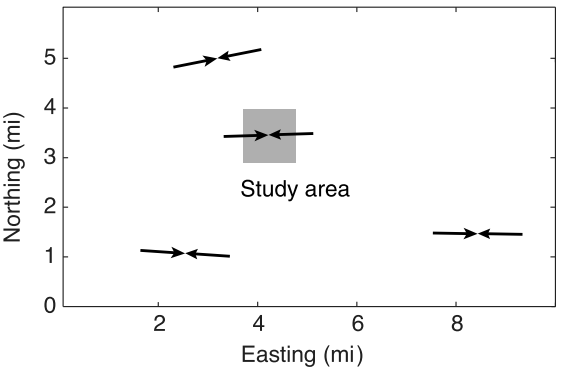

Figure 3. Stress orientations from vertical wells in the study area. In each case, the direction of maximum horizontal stress was determined from dipole sonic logs that were used to obtain the fast-shear velocity direction. In each well, the standard deviation of the measurements is less than 10°. The $S_{H\ max}$ directions are the same as that indicated by the orientation of DITFs shown in Figure 4 as well as other stress indicators in this part of Oklahoma (Alt and Zoback, 2017). The pad being studied is in the shaded area.

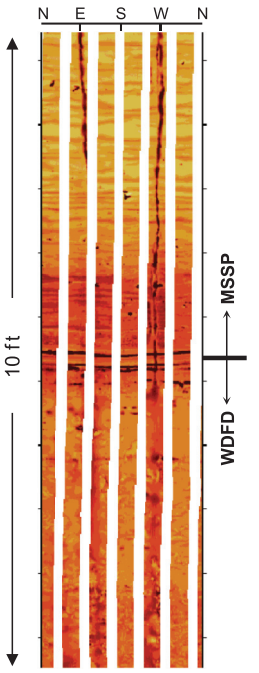

Figure 4. A section of a formation image log of a nearby vertical well that crosses the MSSP and WDFD formation boundary. Note the presence of DITFs trending east–west in the MSSP formation and their disappearance when the well enters the WDFD formation.

Downloaded 03/25/20 to 73.151.200.131. Redistribution subject to SEG license or copyright; see Terms of Use at http://library.seg.org/

this study area) can be obtained from the instantaneous shut-in pressure (ISIP) (Haimson and Fairhurst, 1967) in diagnostic fracture injection tests (DFITs) and the pumping records of each HF treating stage. A limited number of DFITs were conducted in well II, giving reasonable estimation of the $S_{h\ min}$ magnitude within and below the WDFD formation. In this paper, we will use the ISIP as being representative of $S_{h\ min}$, the least principal stress. We recognize that there is some controversy about the appropriate interpretation of HF and DFIT data for determination of $S_{h\ min}$ values in shale formations (e.g., McClure et al., 2016). Obviously, the pressure needed to propagate a hydraulic fracture, sometimes referred to as the *frac gradient*, depends not only on the magnitude of the least principal stress but also on the pumping rate, fluid viscosity, and other factors. However, the HF stimulations reported here were done with low-viscosity slick water, and shut-in was preceded by pumping several hundred barrels of *flush*, slick water without proppant. Although some argue that the ISIP might not be exactly the $S_{h\ min}$ for various reasons, the variations of the ISIP should accurately reflect the variations of the magnitude of the least principal stress acting normal to the HF plane. We also recognize that there can be near wellbore tortuosity that can affect HF pressures (Soliman, 1990), especially in relatively ductile formations (which we revisit in the first part of the "Discussion" section). In the discussions below, we will be focusing on systematic differences in values of the $S_{h\ min}$ in stages with multiple sets of perforations, thus minimizing the effect of near wellbore tortuosity surrounding a particular perforation cluster.

The $S_{h\ min}$ gradient shown by the brown dashed line in Figure 2 is a linear fit to the DFIT measurements in the WDFD and formations below. The ISIPs of the stimulation stages in the MSSP formation (wells A and C) indicate $S_{h\ min}$ magnitude of 25.5 and 27.5 MPa at depths of 5595 and 5590 ft, respectively. ISIPs within well A are quite consistent, and vary by a few MPa in well C. Note that the $S_{h\ min}$ magnitudes measured in wells A and C are consistent with the $S_{h\ min}$ values in the DFIT data at greater depth. In marked contrast, $S_{h\ min}$ values for the WDFD (wells B and D) are systematically higher than those in the MSSP and vary considerably along the wells as indicated by the solid horizontal lines. These variations are discussed in more detail below.

With the constrained S_v and the knowledge of $S_{h\ min}$ in the MSSP, one can check if the S_v and $S_{h\ min}$ difference is bounded by frictional equilibrium in the earth's crust (see Zoback, 2007). For a normal faulting/strike-slip faulting stress state appropriate for this area of Oklahoma (Alt and Zoback, 2017), the lower bound of $S_{h\ min}$ can be estimated via

$$(S_V - P_p)/(S_{h\ min} - P_p) \le [(\mu^2 + 1)^{1/2} + \mu]^2. \quad (1)$$

Within the MSSP, S_V and P_p at stimulation depth are approximately 41 and 17 MPa, respectively. Via equation 1 and assuming the frictional coefficient μ to be approximately 0.6, the value of $S_{h\ min}$ is approximately 25 MPa at the depth of stimulation. Thus, the measured $S_{h\ min}$ magnitudes in the DFITs and HF stages in wells A and C are only slightly above this lower bound, which indicate the MSSP formation is close to normal-faulting frictional equilibrium. Furthermore, the presence of DITFs within the MSSP shown by the FMI logs is an indicator of high horizontal stress anisotropy (see Zoback, 2007). In fact, $S_{H\ max}$ magnitudes that are close to the bound for frictional equilibrium of strike-slip faults:

$$(S_{H\ max} - P_p)/(S_{h\ min} - P_p) \le [(\mu^2 + 1)^{1/2} + \mu]^2. \quad (2)$$

Combining the HF data and DITFs, equations 1 and 2 suggest that $S_{H\ max}$ is significantly larger than $S_{h\ min}$ and quite close to S_v in the MSSP formation, characteristic of a normal/strike-slip stress regime as seen in this part of north-central Oklahoma.

As illustrated in Figure 2 (and shown in more detail below), the values of $S_{h\ min}$ along the two WDFD wells vary between the lower bound indicated by normal-faulting frictional equilibrium (equation 1) and the approximate overburden stress S_v. Combined with the disappearance of the DITFs in the WDFD, it suggests that there is generally less stress anisotropy in the WDFD than in the MSSP (Figure 4).

ISIP VARIATIONS ALONG WOODFORD HORIZONTAL WELLS

Figures 5 and 6 show a variety of data related to the HF stages in the two WDFD wells. The upper part of the figures show the variation of the clay plus kerogen content based on elemental capture spectroscopy (ECS) log (the kerogen content was separately determined derived from the ECS log along with the proprietary information from the data provider). In addition, the ISIP for each HF stage is shown by the red dots and vertical red lines. Note that the ISIP values are sometimes almost as low as the limiting value associated with normal faulting (as seen in the MSSP and the Viola carbonate [VIOL]) but sometimes as high as values approaching, and in one case slightly exceeding, the overburden stress. Note also the strong correlation between the values of ISIP and the clay plus kerogen content.

Figures 5a and 6a also show a strong correlation between the ISIP and the volume of proppant placed during each HF stage (blue bars). For the stages exhibiting higher values of $S_{h\ min}$ than expected, little proppant was successfully placed. In contrast, in stages where $S_{h\ min}$ was relatively low (similar to the values in the MSSP) considerable volumes of proppants were successfully injected. Low proppant delivery suggests either unfavorable fracture path or insufficient fracture aperture width. In either event, the hydraulic fracture stimulation as indicated by the amount of proppant placement and microseismic events distribution (discussed in "Microseismicity indicating heterogeneous stimulation and pad-size faults") is largely dependent on the ISIP magnitude and the clay plus kerogen content.

Figures 5b and 6b show the locations of steeply dipping natural fractures revealed by image logging along the well. There are several intervals of denser fractures seen in the well but there is no apparent correlation with the ISIP values or proppant placement. As shown in Figure 7, most of these fractures are subparallel to each other and oriented approximately in the direction of the $S_{H\ max}$. Most of the fractures dip steeply, although several fractures with lower dips are observed, especially in well B. We consider the density of these fractures to be generally indicative of the lithofacies and the associated stress state (for details, see the "Lithology variations along the Woodford well trajectory" and "Discussion" sections). In certain sections of the wells in which the clay (and organic matter) content is relatively low (such as sections in the WDFD-2) and the density of fractures is higher.

Figures 5c and 6c show the well trajectories (note the exaggerated vertical scale), the locations of the individual stages, and the clay plus kerogen content along the well. The separation of the Woodford into WDFD-1, -2, and -3 facies is in an attempt to better under-

stand the causes of the ISIP variations along the well trajectories (detailed in Section 4).

LITHOLOGY VARIATIONS ALONG THE WOODFORD WELL TRAJECTORY

We used the compositional logs (ECS) to determine the concentrations of silicates, carbonate minerals, and clay and organic matter constituents as a function of depth in the WDFD formation. We subdivide the WDFD into three distinct lithofacies on the basis of clay plus kerogen content (see the discussion in the first part of the "Discussion"). As shown in Figure 8, we define WDFD-1 on the basis of distinctly higher clay plus kerogen than seen in WDFD-2. The WDFD-3 is defined by the very high clay content in the upper 5 ft of the formation. It is worth noting that the thickness of these individual WDFD lithofacies is on the order of merely a few tens of feet.

Compilation of several nearby vertical well logs suggests that these facies are laterally conformable and sequentially consistent. Based on this, it is possible to correlate the lithofacies encountered along the horizontal wells to that identified along the vertical well II. The correlation was facilitated by tracing the ECS signature along the horizontal wells against that of the vertical well. Combining the well geosteering data of the horizontals with the ECS data, we depict the spatial presence of the three WDFD lithofacies with respect to the well trajectory (Figures 5c and 6c). As shown, the local

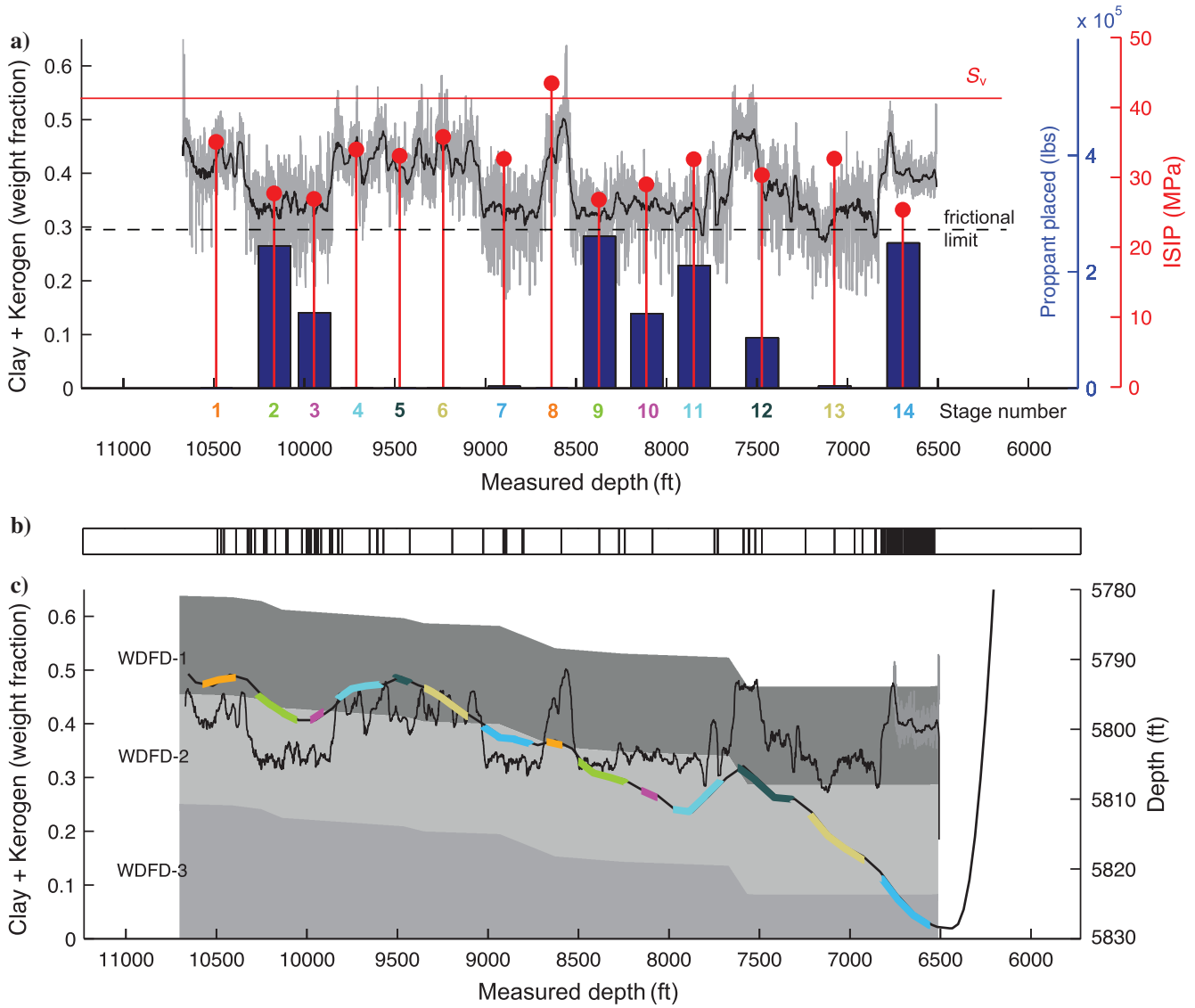

Figure 5. Correlated well information, treatment data, and lithology of horizontal well B: (a) variation of the content of clay plus kerogen (based on ECS log) (black curve represents the smoothed log readings in gray) along the well and its correlation with the ISIP (shown by red dots) and the amount of proppant placed during each HF stage (blue bars). The ISIP and placed proppant amount are shown at the middle of the respective stages. The horizontal red line indicates the magnitude of overburden stress. The dashed black line indicates the magnitude of $S_{h\ min}$ at which normal faulting would occur (see text), (b) the locations of steeply dipping natural fractures along the well, and (c) well trajectory (note the exaggerated vertical scale) and the content of clay plus kerogen (based on ECS) along the well. The separation of the Woodford into the WDFD-1, -2, and -3 lithofacies is explained in the running text.

Downloaded 03/25/20 to 73.151.200.131. Redistribution subject to SEG license or copyright; see Terms of Use at http://library.seg.org/

lithofacies are consistently dipping slightly southeastward. Both horizontal wells penetrated different lithofacies of the WDFD formation along their lengths. In well B, most of stages were located between WDFD facies-1 and -2 (Figure 5c), whereas in well D, most of the stages were placed in WDFD facies-2 and -3 (Figure 6c). In some cases, the perforations associated with a given stage may have been in different lithofacies. It is evident that neither of the WDFD horizontals remained within a constant stratigraphic position with the WDFD (despite the fact that the wells were drilled with only a few tens of feet of vertical drift). Thus, the variations of clay content along both WDFD horizontals are explained by the fact that the trajectories of the wells encounter the three lithofacies defined within the WDFD shale. The depth deviation of the horizontals from the WDFD-2 (presumably easier to be fractured and with less $S_{h\ min}$) causing the lithofacies variations encountered by the well appears to have a significant effect on the effectiveness of the HF of that stage.

MICROSEISMICITY INDICATING HETEROGENEOUS STIMULATION AND PAD-SIZE FAULTS

Microseismic events associated with HF were monitored using 3C geophone arrays deployed at depth in vertical wells I, II, and III. Each of the three monitoring arrays includes 15 levels

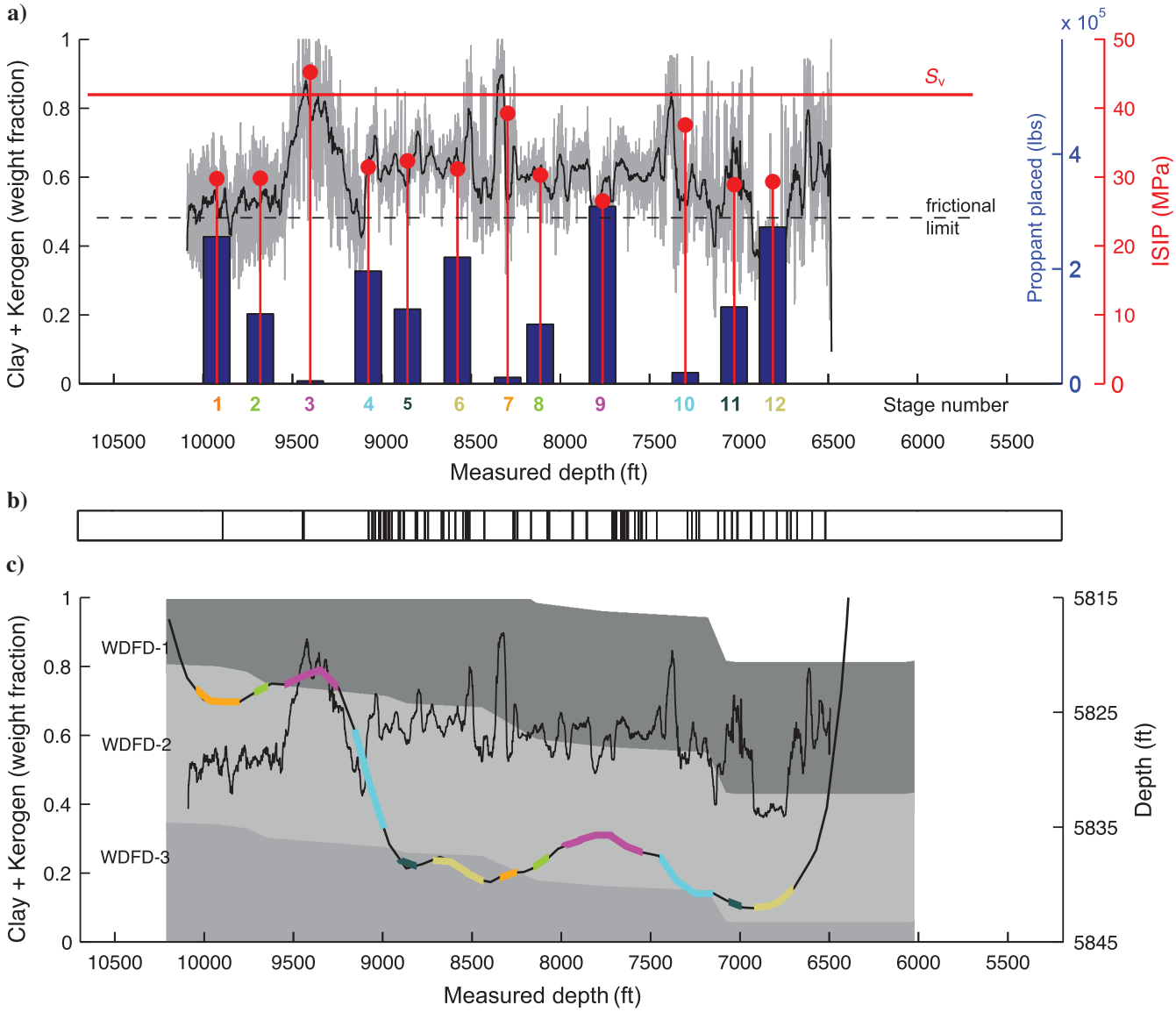

Figure 6. Correlated well information, treatment data, and lithology of horizontal well D: (a) variation of the content of clay plus kerogen (based on ECS log) (black curve represents the smoothed log readings in gray) along the well and its correlation with the ISIP (shown by red dots) and the amount of proppant placed during each HF stage (blue bars). The ISIP and placed proppant amount are shown at the middle of the respective stages. The horizontal red line indicates the magnitude of overburden stress. The dashed black line indicates the magnitude of $S_{h\ min}$ at which normal faulting would occur (see the text), (b) the locations of steeply dipping natural fractures along the well, and (c) the well trajectory (note exaggerated vertical scale) and the content of clay plus kerogen (based on ECS) along the well. The separation of the Woodford into WDFD-1, -2, and -3 lithofacies is explained in the running text.

Downloaded 03/25/20 to 73.151.200.131. Redistribution subject to SEG license or copyright; see Terms of Use at http://library.seg.org/

Downloaded 03/25/20 to 73.151.200.131. Redistribution subject to SEG license or copyright; see Terms of Use at http://library.seg.org/

of geophones, spanning a depth range of approximately 400 ft above and below the depth of the horizontal wells (Figure 1). The wells were stimulated in the following order: well B > A > C > D. Each well was hydraulically fractured from toe to heel using the plug-and-perf technique between 12 and 15 stages. There were a total of 8865 microseismic events detected and located by the microseismic service company during the stimulation of the four horizontal wells. Figure 9a shows the map view of all the located events, regardless of their magnitudes. Figure 9b shows only those events recorded on all three monitoring arrays. Ideally, an elongated cloud of events trending in the $S_{H\ max}$ direction from the perforation locations (Fisher et al., 2004; Maxwell, 2014) presumably surrounds the hydraulic fractures emanating from each perforation cluster. In the case of the wells studied here, one would expect east–west clouds of events associated with each HF stage. It is obvious that this is not the case for the great majority of HF stages. Events are unevenly distributed, with very few events along significant sections of each well and there are many events clustered in the vicinity of the three observation wells. As low-magnitude events are likely to be recorded only by nearby arrays (Warpinski et al., 2009; Maxwell, 2014), it is important to note that the heterogeneous distribution of events is shown in Figure 9a and 9b, indicating that the clustering of events near the monitoring arrays is not an artifact of detecting small magnitude events near the arrays but fewer small events elsewhere.

One clue to the uneven distribution of events can be seen by the unusual trends of events associated with the HF stages in each well (Figure 10, events colored by stage). Note that there is a persistent east–west-trending cluster of events seen near the toe of well A and to the north of observation well I. Because hydraulic fractures and active normal faults are expected to trend east–west, it is obviously difficult to distinguish whether a group of east–west-trending microseismic events indicate the expected cloud of microseismic

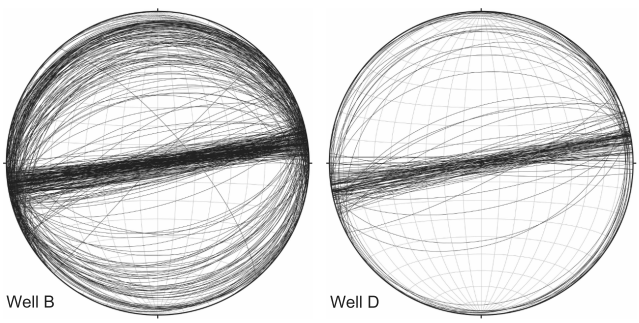

Figure 7. Stereonets display the orientations of fractures and faults identified from the borehole image log along Woodford wells B and D. Nearly all of the fractures and faults strike approximately N85°E and dip steeply, although well B contains more subhorizontal fractures.

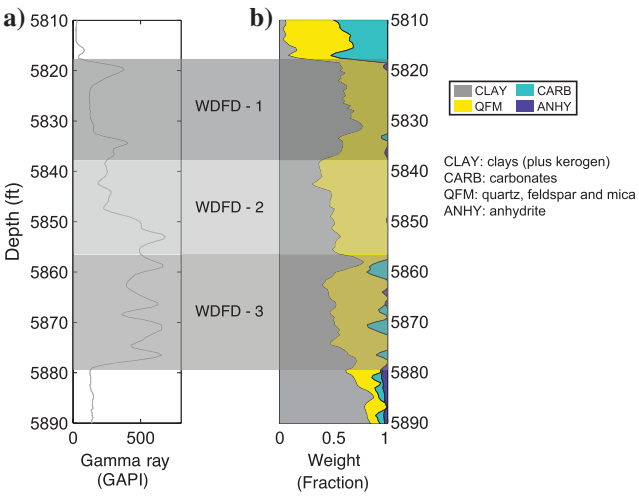

Figure 8. Geophysical logs of the vertical well II: (a) natural gamma ray log and (b) ECS log representing the composition of major constituent minerals by weight fraction. The WDFD has been separated into lithofacies WDFD-1, -2, and -3 based on the relative abundance of high clay plus kerogen (and relatively low quartz, feldspar, and mica) in WDFD-1 and -3 compared with WDFD-2.

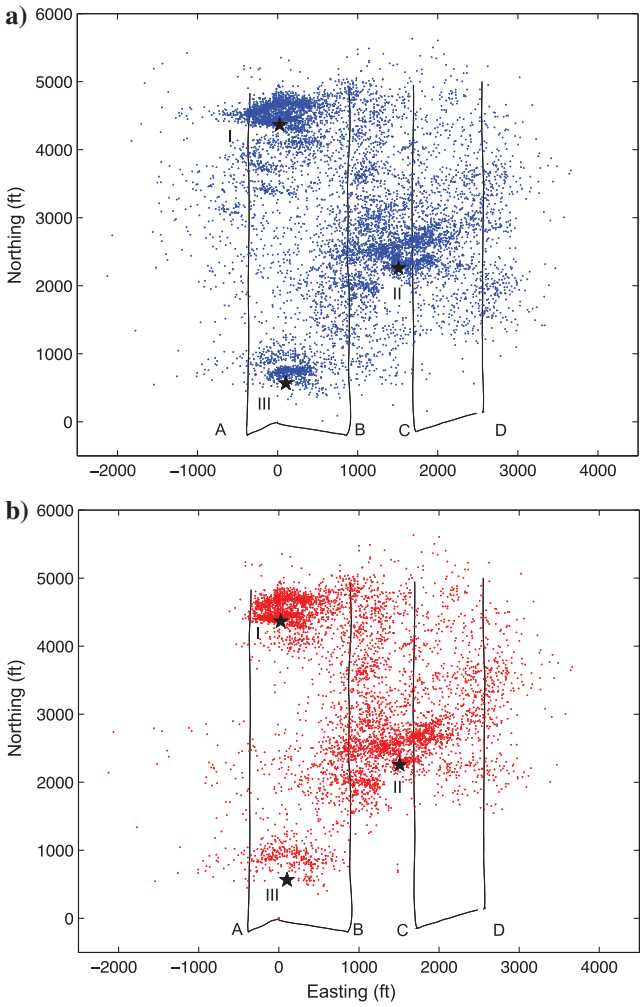

Figure 9. Map view of the study area and configuration of four horizontal wells (A, B, C, and D) and three observation wells (I, II, and III, indicated by the black stars) and the locations of the microseismic events reported by the service provider: (a) all events (as detected by any of the three arrays) as shown by the blue dots and (b) events detected by all three arrays shown by the red dots. Note that the dense clusters of events near the three recording wells in (a) are also seen in (b) indicating that they are not artifacts associated with the detection of very small events only near the recording arrays.

Downloaded 03/25/20 to 73.151.200.131. Redistribution subject to SEG license or copyright; see Terms of Use at http://library.seg.org/

events surrounding a hydraulic fracture or slip on small-scale faults in the damage zone of a larger, pad-scale normal fault (e.g., Farghal and Zoback, 2014). Because the east–west-trending microseismic events near the toe of well A are seen even when distant wells C and D were stimulated, we interpret there to be a pad-scale east–west-trending normal fault in this area, which we delineate as fault F1. It is interesting in the microseismic cross sections seen Figure 11 that there are events in the WDFD formation associated with F1 when the MSSP was being stimulated. We would not normally expect a stimulated hydraulic fracture to propagate from the low stress MSSP to the higher stress WDFD formation.

Figure 11 also shows that HF of stages 3–7 (between 3100 and 4300 ft of northing) in MSSP well A triggered events in the MSSP and the underlying WDFD formation. In map view (Figure 10a), these events form several subparallel, east–west-trending clouds, which resemble the expected pattern as a result of HF. However, events associated with stages 3, 4, and 5 in well A partition themselves into multiple east–west-trending clouds that are outside the stimulated zone, which is not expected for hydraulic fractures. Therefore, we hypothesize that there appears to be a group of subparallel small-scale normal faults that we label F2. Again, as the least principal stress is higher in the WDFD than the MSSP, downward propagation of hydraulic fractures from the MSSP to the WDFD would not be expected, providing additional support for at least some of the microseismic events to be associated with faults connecting the MSSP and WDFD formations.

Besides east–west-trending normal faults, we also expect near vertical N60°E and S60°E strike-slip faults to be active in this area, as illustrated in sketch in Figure 12. There are clusters of events across the middle of wells B and C that also appear to delineate a fault (marked as F3 in Figures 10 and 11), which correlate with locations along the well in which there is significant vertical distribution of microseismic events seen in cross section (Figure 11). The events are pervasive across the MSSP and WDFD and even occur above the MSSP. On the map view (Figure 10), these densely populated events are associated with wells B and C and can also be seen distinctly in Figure 9.

There is also a dense population of east–west-trending events to the north of the observation well III when well A was stimulated during stages 13–15 (Figure 10). These somewhat isolated events occurred at this location when wells B and C were stimulated. In addition, nearly all of these events clouds appear to vertically connect the MSSP and WDFD (Figure 11), which is not expected for the MSSP well C. We interpret this to mean there is a another east–west-trending normal fault (marked as F4) in this area.

It is worthwhile to note that the stress variations along the WDFD wells B and D also affect the distribution of microseismic events. For WDFD well B, significant upward propagation is observed for some stages, which is not surprising as stated earlier one would expect HF propagation from formations with high stress to those with low. It is interesting, however, that the stages in well B with abnormally high ISIP values (1, 4, 5, 6, 7, 8, and 13 as shown in Figure 5a) are associated with almost no microseismic events upward propagation except in the areas where preexisting faults were encountered. Similarly, in well D, for stages with abnormally high ISIP values (3, 7, and 10 as shown in Figure 6a) upward propagation into the MSSP seems to be limited to stage 3, which is associated with fault F1.

To confirm the presence of faults cutting across the pads, we sought to extract discontinuous features from the available 3D seismic reflection data using ant tracking (Randen et al., 2001; Farghal and Zoback, 2014). The variance attribute of the seismic data was calculated and processed through two passes of ant tracking to enhance any discontinuities. The result of the ant tracking is shown in Figure 12 from a cut-out view of a horizon near the depth of both WDFD wells. Cross-cutting discontinuities resembling faults emerge at locations where faults F2, F3, and F4 were identified from microseismic events. Notably, F2 is indeed composed of several, subparallel small-scale faults, coinciding with the relevant

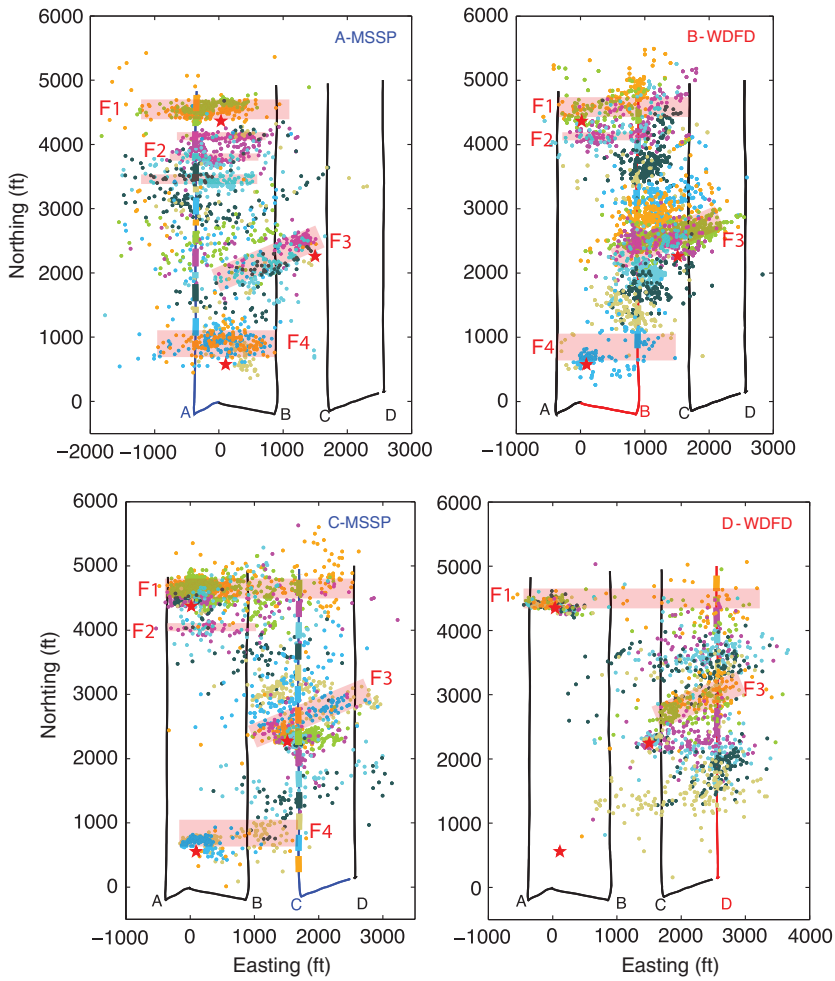

Figure 10. Map view of microseismic events locations for each well, colored by stage. Events potentially associated with slip of on preexisting faults are indicated by the red shaded areas and discussed in the text. The red stars indicate the locations of the observation wells.

microseismic trends identified in well A. One of the faults in F2 extending across the pad and cutting through all four wells was not previously recognized on the microseismic data. As expected, F3 are nearly vertical and favorably oriented with respect to $S_{H\ max}$ direction (forming an angle between 20° and 30°). Again, F4 is as expected a steeply inclined fault dipping at approximately 70° toward $S_{h\ min}$.

Some of the faults (F2 and F3) are also evident on the available borehole images of two WDFD horizontals. One branch of F2 and the F3 was identified as fault zones in well B at the measured depth of approximately 8990 and 8230 ft, respectively. The image log of well B does not cover the location where F4 is located.

It is worth noting that although fault F1 is not visible on the 3D seismic data in the sampled horizons, the spatial and temporal correlation between the events and the stimulation of distant wells strongly suggests the presence of a fault zone. It is also worth noting in Figure 12 that the pattern of normal and strike-faults seen in the seismic data that correlate with faults F1–F4 is also seen to the north of the wells, as expected for a strike-slip/normal faulting area.

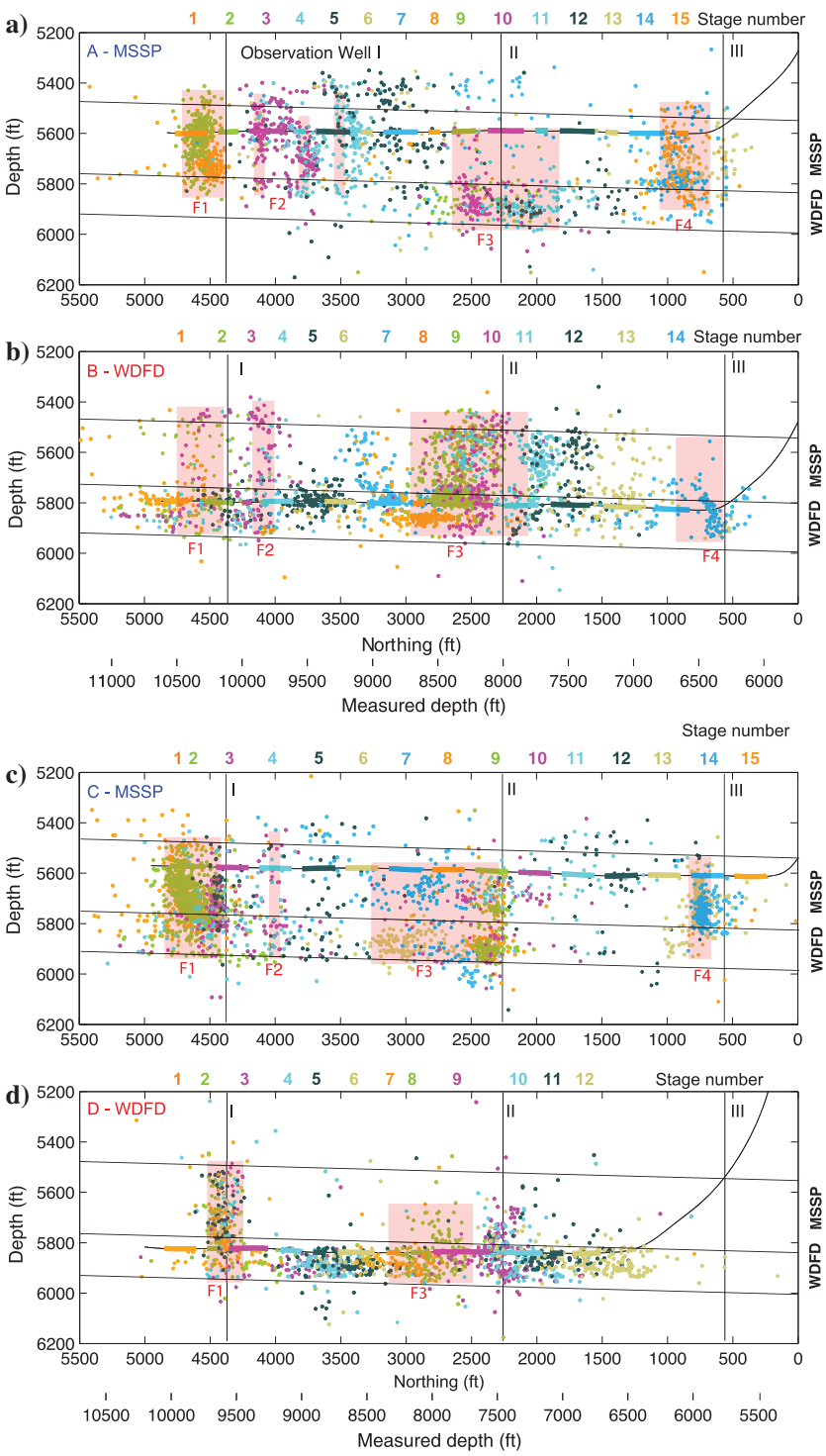

Figure 11. Cross-sectional view of microseismic events locations associated with the HF stages in each of the four horizontal wells. The events are colored according to stages. Events potentially associated with slip of preexisting faults are indicated by the red shaded areas and discussed in the text. The vertical lines represent observation wells.

DISCUSSION

Correlation between lithology, ISIP, and HF effectiveness

Figures 5c and 6c show the content of compliant components (clay and organic matter) along the horizontal section of the wells B and D, respectively, which positively correlate with the ISIP (reflecting $S_{h\ min}$) at the perforated stages. The variations of $S_{h\ min}$ with lithology can be explained by viscoplastic stress relaxation (Sone and Zoback, 2013b, 2014b). As demonstrated by Sone and Zoback (2013a, 2014a), the abundance of compliant components (clay and organic matter) relative to stiff components (silicate and carbonate minerals) control the degree of viscoplastic creep and stress relaxation in organic-rich shale formations. Sone and Zoback (2014a, 2014b) show in the Barnnet Shale that the difference between the overburden stress and least principal stress decreases with the abundance of the compliant component content causing the frac gradient to increase. Warpinski et al. (1985) and Warpinski and Teufel (1989) present a vertical profile of many least principal stress measurements with depth in the Piceance Basin of Colorado. They find that the least principal stress increases significantly within shale formations and can approach the vertical stress, even in a normal faulting environment.

Fundamentally, the presence of compliant components induces viscoplastic stress relaxation reduces the difference between the vertical stress and horizontal stress thereby increasing the frac gradient, the pressure above the least principal stress needed to propagate a hydraulic fracture. According to Sone and Zoback (2014b),

Downloaded 03/25/20 to 73.151.200.131. Redistribution subject to SEG license or copyright; see Terms of Use at http://library.seg.org/

Downloaded 03/25/20 to 73.151.200.131. Redistribution subject to SEG license or copyright; see Terms of Use at http://library.seg.org/

smaller ($S_v - S_{h\ min}$) in clay-rich lithologies also limits the extent of horizontal stress anisotropy ($S_{H\ max} - S_{h\ min}$). This is consistent with the disappearance of DITFs in the WDFD, as an indicator of lower degree of horizontal stress anisotropy, as the vertical borehole reaches the clay-rich WDFD formation (Figure 4).

Apart from the stress variations, lithology variations also affect the effectiveness of HF. Lithology variations lead to changes in the mechanical properties of rocks (Sone and Zoback, 2013a, 2013b), which have often been loosely related to brittleness (or ductility) (e.g., Rybacki et al., 2016). Shales containing higher amounts of compliant components (e.g., clay minerals and organic matter) are generally less brittle (e.g., Abousleiman et al., 2016). Theoretically, ductile materials under tensile stress loading tend to undergo yielding rather than fracturing in a brittle fashion considering the plastic deformation at the crack tip (Janssen et al., 2006). This implies more ductile lithologies are more resistant to HF, and more brittle lithologies are expected to contain more tensile fractures, whether they occur in nature or under human perturbation. The fact that in the stages associated with high ISIPs, the microseismic events exhibited little vertical growth (Figure 11) provide support for lithology affecting the in situ stress and HF effectiveness. The observed variations of the ISIP are not correlated with the sequence of the HF treatment stages (wells B and D were treated from the toe to the heel). Thus, the sequence of HF treatments and the associated "stress shadow" due to proppant or poroelastic effects (Soliman et al., 2008; Vermylen and Zoback, 2011) do not account for the variations of ISIP.

In situ stress in high-clay facies

It is particularly intriguing that how the hydraulic fractures initiate and propagate within high-clay facies of the WDFD (WDFD-1 and WDFD-3) where the in situ stress and lithology contrast with those in the relatively low-clay facies (WDFD-2). Figures 5c and 6c show that because of the tortuous trajectories, certain stages of wells B and D feature relatively high-clay facies below and above the targeted WDFD-2 facies. It is in those stages that the ISIPs are anomalously high and sometimes comparable with the overburden stress S_V. The high ISIP suggests that the least principal stress (or the minimum horizontal stress) is, in fact, close to the overburden stress. The assumption that ISIP reflects the least principal stress requires the created hydraulic fractures to open against the least resistance (Hubbert and Willis, 1957). The exact orientation and geometry of the hydraulic fracture are difficult to infer. It is possible that at small scales, hydraulic fractures may locally deviate from being perpendicular to the far-field least principal stress (usually $S_{h\ min}$) due to an inclined well trajectory, stress redistribution near the wellbore, and preexisting discontinuities intersecting the wellbore (Soliman, 1990), but at larger scales, the effect of preexisting discontinuities (including bedding) is less prominent and hydraulic fractures are generally oriented normal to the least principal stress.

As mentioned above, the presence of compliant components induces viscoplastic stress relaxation, which reduces the overall stress anisotropy. The fact that the ISIP is close to the overburden stress in a normal/strike-slip faulting environment, in large measure, is indicative of a quasi-isotropic stress state ($S_V \sim S_{H\ max} \sim S_{h\ min}$), which is consistent with the disappearance of DITFs along vertical wellbores in the certain lithofacies of the WDFD formation (e.g., WDFD I) (Figure 4).

We hypothesize that the interaction between the quasi-isotropic stress state and compliant lithology may have locally inhibited the fracture growth and may have induced a rather complicated fracture geometry near the wellbores. Accordingly, the locally tortuous fracture path and the interaction with preexisting discontinuities might have consumed most of the stimulation energy and rendered the HF ineffective (Warpinski and Teufel, 1989; Suarez-Rivera et al., 2016).

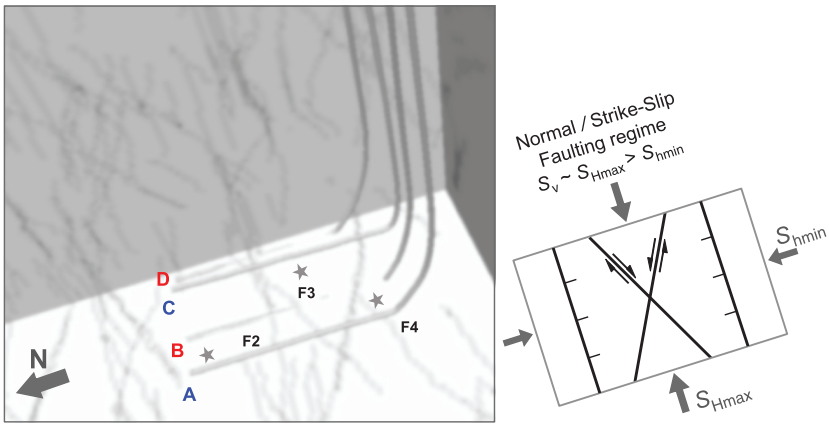

Figure 12. Three-dimensional rendering of the enhanced discontinuities using ant tracking (based on the variance attribute) of 3D seismic data. The locations where the observation wells intersect the shown horizon are marked with stars. Note those fault-like structures (labeled as F2, F3, and F4) intercept certain parts of the wells, and their traces agree with the microseismic event trends. As shown by the cartoon on the right, the trends of the faults are consistent with the expected trends of active faults in a normal/strike-slip faulting stress regime representative of this part of Oklahoma (Alt and Zoback, 2017) and the observed stress orientation.

CONCLUSIONS

An integrated analysis of geologic, geomechanical, geophysical, and microseismic monitoring data has helped us to understand the highly variable effectiveness of multistage HF stimulation in two wells in the Woodford Formation. We found that HF stimulation effectiveness is primarily affected by the heterogeneity of the reservoir, which manifests in two ways. First, it is composed of lithologically and mechanically unique lithofacies. Specifically, the abnormally high frac gradients occur in stages in which the trajectories of the wells encounter clay-rich lithofacies. The abundance of clay contributes to time-dependent rock deformation through viscoplastic flow, which is considered to have modified the in situ stress over geologic time. The correlation between stress and lithology was hitherto unaccounted in the conventional analysis of HF. Second, we found that preexisting, pad-scale faults frequently divert fracturing fluids and limits the ability of HF operations to stimulate production. Nearly all of the faults delineated by the microseismic events revealed themselves as discontinuous features based on 3D seismic reflection data. It is clear that the landing points and trajectories of the horizontal wells and the perforation locations should be carefully planned and

Downloaded 03/25/20 to 73.151.200.131. Redistribution subject to SEG license or copyright; see Terms of Use at http://library.seg.org/

placed by considering lithologic variations and the presence of preexisting faults.

The inherent lithologic variations of the WDFD formation, lithologic-induced stress changes, and the presence of preexisting faults result in ineffective HF stimulation along much of the well paths. In well B, for example, seven of the 14 frac stages were unsuccessful because the well path was in the wrong lithofacies. Apparently, the analysis considering reservoir heterogeneity, rock time dependency, and formation-scale discontinuity was not routinely incorporated in the practice of HF stimulation. As a case study, this paper calls for attention to these characteristics. Future work is warranted to understand the underlying mechanism of stress evolution with viscous relaxation in the various lithofacies to facilitate a more quantitative analysis for effective HF stimulation.

ACKNOWLEDGMENTS

This study was supported by data and funding from the Devon Energy Corp., and the Stanford Rock Physics and Borehole Geophysics Project (SRB). G. Alalli, N. Farghal, and H. Arévalo helped the 3D seismic data processing and interpretation.

NOMENCLATURE

P_p	=	pore pressure
S_V	=	vertical stress
$S_{H\ max}$	=	maximum horizontal stress
$S_{h\ min}$	=	minimum horizontal stress
S_3	=	least principal stress
μ	=	frictional coefficient

REFERENCES

Abousleiman, Y. N., K. L. Hull, Y. Han, G. Al-Muntasheri, P. Hosemann, S. Parker, and C. B. Howard, 2016, The granular and polymer composite nature of kerogen-rich shale: Acta Geotechnica, **11**, 573–594, doi: 10.1007/s11440-016-0435-y.

Alt, R. C., and M. D. Zoback, 2017, In-situ stress and active faulting in Oklahoma: Bulletin of the Seismological Society of America, **107**, 216–228, doi: 10.1785/0120160156.

Farghal, N. S., and M. D. Zoback, 2014, Utilizing ant-tracking to identify slowly slipping faults in Barnett Shale: Presented at the Unconventional Resources Technology Conference, SPE/AAPG/SEG.

Fisher, M., J. Heinze, C. Harris, C. Wright, and K. Dunn, 2004, Optimizing horizontal completion techniques in the Barnett shale using microseismic fracture mapping: Presented at the SPE Annual Technical Conference and Exhibition, SPE-90051.

Haimson, B. C., and C. Fairhurst, 1967, Initiation and extension of hydraulic fractures in rock: SPE Journal, **7**, 310–318, doi: 10.2118/1710-PA.

Hubbert, M. K., and D. G. Willis, 1957, Mechanics of hydraulic fracturing: Journal of Petroleum Technology, **13**, 371–376.

Janssen, M., J. Zuidema, and R. J. H. Wanhill, 2006, Fracture mechanics, 2nd ed.: VSSD.

Ma, X., and M. D. Zoback, 2017, Lithology variations and cross-cutting faults affect hydraulic fracturing of Woodford Shale: A case study: Presented at the Hydraulic Fracturing Technology Conference and Exhibition, SPE.

Maxwell, S., 2014, Microseismic imaging of hydraulic fracturing: Improved engineering of unconventional shale reservoirs: SEG Distinguished Instructor Series 17.

McClure, M. W., H. Jung, D. D. Cramer, and M. M. Sharma, 2016, The fracture-compliance method for picking closure pressure from diagnostic fracture-injection tests: SPE Journal, **21**, 1321–1339, doi: 10.2118/179725-PA.

Nelson, P. H., and N. J. Gianoutsos, 2014, Potentiometric surfaces for seven stratigraphic units and an explanation for underpressure in the Greater Anadarko Basin, Oklahoma, Texas, Kansas, and Colorado, *in* D. K. Higley, ed., Petroleum systems and assessment of undiscovered oil and gas in the Anadarko Basin Province, Colorado, Kansas, Oklahoma, and Texas — USGS Province 58: U.S. Geological Survey Digital Data Series.

Randen, T., S. Pedersen, and L. Sønneland, 2001, Automatic extraction of fault surfaces from three-dimensional seismic data: 71st Annual International Meeting, SEG, Expanded Abstracts, 551–554.

Rybacki, E., T. Meier, and G. Dresen, 2016, What controls the mechanical properties of shale rocks? Part II: Brittleness: Journal of Petroleum Science and Engineering, **144**, 39–58, doi: 10.1016/j.petrol.2016.02.022.

Soliman, M. Y., 1990, Interpretation of pressure behavior of fractured, deviated, and horizontal wells: Presented at the Latin America Petroleum Engineering Conference, SPE.

Soliman, M. Y., L. East, and D. Adams, 2008, Geomechanics aspects of multiple fracturing of horizontal and vertical wells: SPE Drilling & Completion, **23**, 217–228, doi: 10.2118/86992-PA.

Sone, H., and M. D. Zoback, 2013a, Mechanical properties of shale-gas reservoir rocks — Part 1: Static and dynamic elastic properties and anisotropy: Geophysics, **78**, no. 5, D381–D392, doi: 10.1190/geo2013-0050.1.

Sone, H., and M. D. Zoback, 2013b, Mechanical properties of shale-gas reservoir rocks — Part 2: Ductile creep, brittle strength, and their relation to the elastic modulus: Geophysics, **78**, no. 5, D393–D402, doi: 10.1190/geo2013-0051.1.

Sone, H., and M. D. Zoback, 2014a, Time-dependent deformation of shale gas reservoir rocks and its long-term effect on the in situ state of stress: International Journal of Rock Mechanics & Mining Sciences, **69**, 120–132, doi: 10.1016/j.ijrmms.2014.04.002.

Sone, H., and M. D. Zoback, 2014b, Viscous relaxation model for predicting least principal stress magnitudes in sedimentary rocks: Journal of Petroleum Science and Engineering, **124**, 416–431, doi: 10.1016/j.petrol.2014.09.022.

Suarez-Rivera, R., J. Graham, S. Ali, J. Degenhardt, and A. Jegadeesan, 2016, Optimizing lateral landing depth for improved well production: Presented at the Unconventional Resources Technology Conference, SPE/AAPG/SEG.

Vermylen, J. P., and M. D. Zoback, 2011, Hydraulic fracturing, microseismic magnitudes, and stress evolution in the Barnett Shale, Texas, USA: Presented at the Hydraulic Fracturing Technology Conference and Exhibition, SPE.

Warpinski, N. R., P. Branagan, and R. Wilmer, 1985, In-situ stress measurements at U. S. DOE's multiwell experiment site, Mesaverde Group, Rifle, Colorado: Journal of Petroleum Technology, **37**, 527–536, doi: 10.2118/12142-PA.

Warpinski, N. R., M. J. Mayerhofer, M. C. Vincent, C. L. Cipolla, and E. P. Lolon, 2009, Stimulating unconventional reservoirs: Maximizing network growth while optimizing fracture conductivity: Journal of Canadian Petroleum Technology, **48**, 39–51, doi: 10.2118/114173-PA.

Warpinski, N. R., and L. W. Teufel, 1989, In-situ stresses in low-permeability, nonmarine rocks: Journal of Petroleum Technology, **41**, 405–414, doi: 10.2118/16402-PA.

Zoback, M. D., 2007, Reservoir geomechanics: Cambridge University Press.